Imperfection Surveys on a 10-ft-Diameter Shell Structure

Johann Arbocz*
Northrop University, Inglewood, Calif.
and
Jerry G. Williams†
NASA Langley Research Center, Hampton, Va.

The results of an extensive imperfection survey on a 10-ft-diameter integrally stiffened cylindrical shell are presented. The shape of the measured initial imperfections is clearly influenced by details of the shell construction. The modal components of the measured imperfection surface as a function of the circumferential and of the axial wave numbers are calculated. The discrete axial power spectral density functions and the corresponding root-mean-square values of the imperfections are also determined for given circumferential wave numbers. Using the Fourier coefficients of the measured initial imperfections, buckling loads are calculated by solving the nonlinear Donnell-type imperfect shell equations iteratively. The calculated lowest buckling load compares favorably with the values usually recommended for similar shell structures.

Nomenclature

A = cross-sectional area of stiffener, in.^{2}
$A_{io}, A_{k\ell}, B_{k\ell}$ = coefficients of the half-wave cosine Fourier representation, see Eq. (1)
c = Poisson's effect, $c=\sqrt{3(1-\nu^2)}$
$C_{k\ell}, D_{k\ell}$ = coefficients of the half-wave sine Fourier representation, see Eq. (2)
d = distance between stiffeners, in.
e = distance between centroid of stiffener cross section and middle surface of skin, in.
E = Young's modulus, lb/in.^{2}
i,k = number of half-waves in the axial direction
$i_{c\ell}$ = number of half-waves in the classical axisymmetric buckling mode for isotropic shells
I = moment of inertia of stiffener cross section about its centroidal axis, in.^{4}
ℓ = number of full waves in the circumferential direction
L = shell length, in.
M_x = moment resultant, in. lb/in.
N_x = stress resultant, lb/in.
N_{xSS-3} = perfect shell buckling load using membrane prebuckling analysis and SS-3 boundary conditions, lb/in.
$p(\bar{\omega})$ = power spectral density function, in., see Eq. (A8)
R = shell radius, in.
$S(\omega)$ = nondimensional power spectral density function, see Eq. (A12)
t = shell thickness, in.
v = in-plane displacement in the circumferential direction
w = radial displacement (positive outward)
$\bar{w}$ = radial imperfection from perfect circular cylinder (positive outward)
$\bar{W}$ = nondimensional radial imperfection, $\bar{W}=\bar{w}/t$
x,y = axial and circumferential coordinates on the middle surface of the shell, respectively
Y_1, Z_1 = coordinates locating origin of best-fit cylinder reference axis, see Fig. 3
α, β = mode shape parameters
Δ^2 = root-mean-square value of the measured imperfections
ϵ_1, ϵ_2 = small angles in radians denoting inclination of best-fit reference axis, see Fig. 3
ν = Poisson's ratio
$\hat{\xi}$ = equivalent initial imperfection amplitude, see Fig. 7
ρ_s = nondimensional loading parameter $=N_x/[(E/c)(t^2/R)]$
$\bar{\omega}_o$ = fundamental spatial frequency, $=\pi/L$
ω = nondimensional spatial frequency, $=k/i_{c\ell}$

Subscripts

r = ring
s = stringer

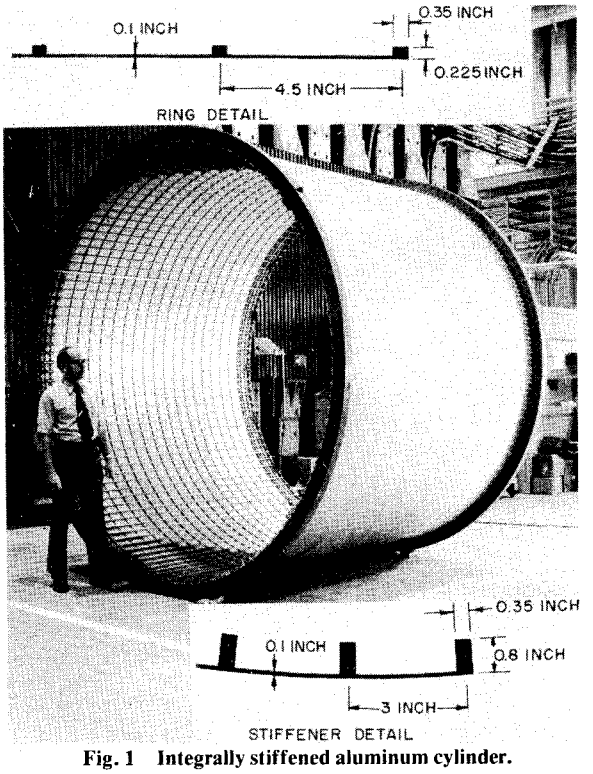

Fig. 1 Integrally stiffened aluminum cylinder.

Received July 27, 1976; revision received Feb. 14, 1977.
Index category: Structural Stability.

*Associate Professor of Aeronautics (also Senior Research Fellow in Aeronautics, California Institute of Technology, Pasadena, California); presently Professor of Aircraft Structures, Delft University of Technology, The Netherlands. Member AIAA.

†Aerospace Engineer. Member AIAA.

Introduction

FOR axially compressed cylindrical shells initial geometric imperfections have come to be accepted qualitatively as the explanation for the disagreement between the analytical predictions of the buckling load and the experimental values and for the frequently large scatter of the experimental results. At the same time, the necessary analytic tools for rigorous buckling load calculations based on measured initial imperfections have also been developed.[1,2] The accuracy and reliability of these methods have been demonstrated on tests conducted with laboratory-scale specimens.[2,3] Hence, with current analytic capability, it now appears possible to closely predict the strength of many classes of structures *if the critical components of the initial imperfection are known.*

Thus, in order to incorporate the idea of imperfection sensitivity into engineering practice, it is necessary to be able to answer the question: "What imperfections are likely to exist in practical aerospace structures?" As a first step toward providing some information about actual imperfections, this paper describes the results of a detailed imperfection survey carried out on a 10-ft-diam integrally stiffened cylindrical shell. The paper also contains buckling load calculations based on the measured initial imperfections.

Experimental Program

Test Specimen

The aluminium cylindrical shell on which initial imperfections were measured is shown in Fig. 1. The outside diameter of the cylinder is 120.89 in. and it is 94 in. long. The cylinder skin is 0.1 in. thick and is integrally stiffened by 0.8-in.-deep × 0.35-in.-wide longitudinal stiffeners and by 0.225-in.-deep × 0.35-in.-wide rings. The cylinder was constructed from three integrally machined 1.0-in.-thick flat plates that were rolled to a 60.0 in. radius and welded together along a stiffener. Since each plate was bounded by a complete stiffener, a longitudinal stiffener of double thickness resulted at the three junctions. See Table 1 for the corresponding nondimensional parameters of the shell.

A steel end ring (2.5 in. wide × 3.5 in. deep) was attached to the outer surface at each end of the cylinder. The end rings were machined with an inside diameter 0.010 in. larger than the outside diameter of the cylinder. The inside and outside diameters of the end rings were concentric and machined to a 64 rms finish. The outside diameter dimensions of the two end rings matched to within 0.006 in. The end rings were attached to the cylinder using bolts and attachment plates mounted inside the cylinder.

Test Equipment and Test Procedure

The equipment used to carry out the initial imperfection surveys on the cylinder is shown in Fig. 2. The technique employed measured the deviation of the cylinder outer surface relative to an imaginary cylindrical reference surface. Physically, this was accomplished with a 10-ft-long aluminium guide rail supported on the outside diameter of the two steel end rings and a direct current differential transformer (DCDT) instrument on a trolley car. The trolley car had steel roller bearing wheels and was spring loaded to roll with continuous contact along the guide rail. The car was slowly driven along the guide rail by an electric motor. The position of the car was electronically measured using a potentiometer that rotated as the car moved along the track. Accuracy of the displacement measurements was to within ±0.002 in.

Table 1 Geometric properties of the shell

t = 0.10 in.	d_s	= 3.0 in.	d_r	= 4.5 in.
L = 81.0 in.	$A_s/d_s t$	= 0.933	$A_r/d_r t$	= 0.175
R/t = 600	$I_s/d_s t^3$	= 4.978	$I_r/d_r t^3$	= 0.074
L/R = 1.35	e_s/t	= 4.5	e_r/t	= 1.625

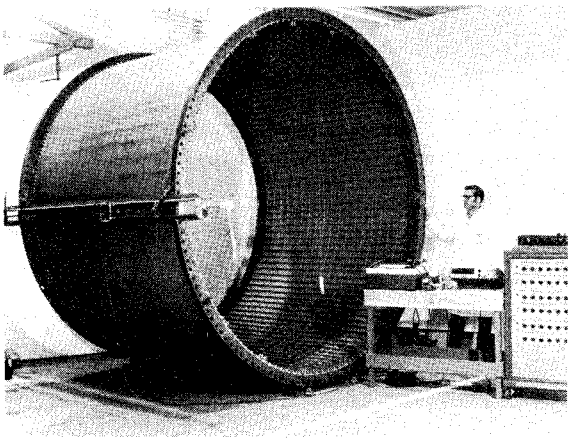

Fig. 2 Initial imperfection survey instrumentation.

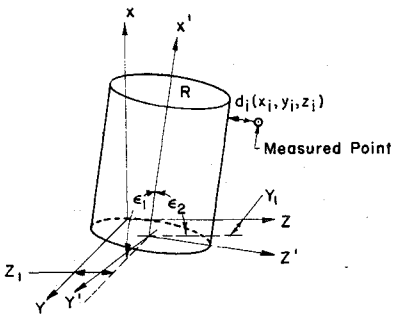

X,Y,Z Reference axis of traversing pick-up
X',Y',Z' Reference axis of best fit cylinder
d_i Normal distance from measured point to best fit cylinder

Fig. 3 Definition of the "perfect" cylinder.

Surveys were made along the cylinder length for a distance of 81 in. (6.5 in. at each end of the cylinder were not measured). The guide rail was moved stepwise around the cylinder circumference in 5-deg increments thus yielding a total of 72 discrete scans for the complete cylinder. Some scans were performed more than once to determine the repeatability of the measurements. Repeatability of the data was found to be within the tolerance limits of the measuring equipment.

The data was recorded using two methods: 1) continuously with an x-y recorder in which the deviation from a neutral position (to the reference surface) was plotted as a function of position along the cylinder length and 2) discretely digitized and recorded on magnetic tape. Discrete digital data was recorded every 0.236 in. along the cylinder length, thus yielding 343 data points for a typical 81-in. scan. Discrete data acquisition was triggered by a phototube circuit that was opened and closed by a notched disk, which rotated as the trolley car traversed along the guide rail. The digitized data was then used for data reduction.

Data Reduction

Before an initial imperfection can be determined, it is necessary to define the perfect shell. In the experiment, the radial deviations from the imaginary cylindrical reference surface, defined by the two very accurately machined steel end rings and the rigid aluminium rail connecting them, were measured. Next the data reduction program described in Ref. 4 was used to find the best-fit cylinder to the measured data of the initial imperfection scan. Using the method of least squares, this program computed the eccentricities Y_1 and Z_1, the rigid body rotations ϵ_1 and ϵ_2, and the mean radius R (see Fig. 3). Finally, the measured displacements were recomputed

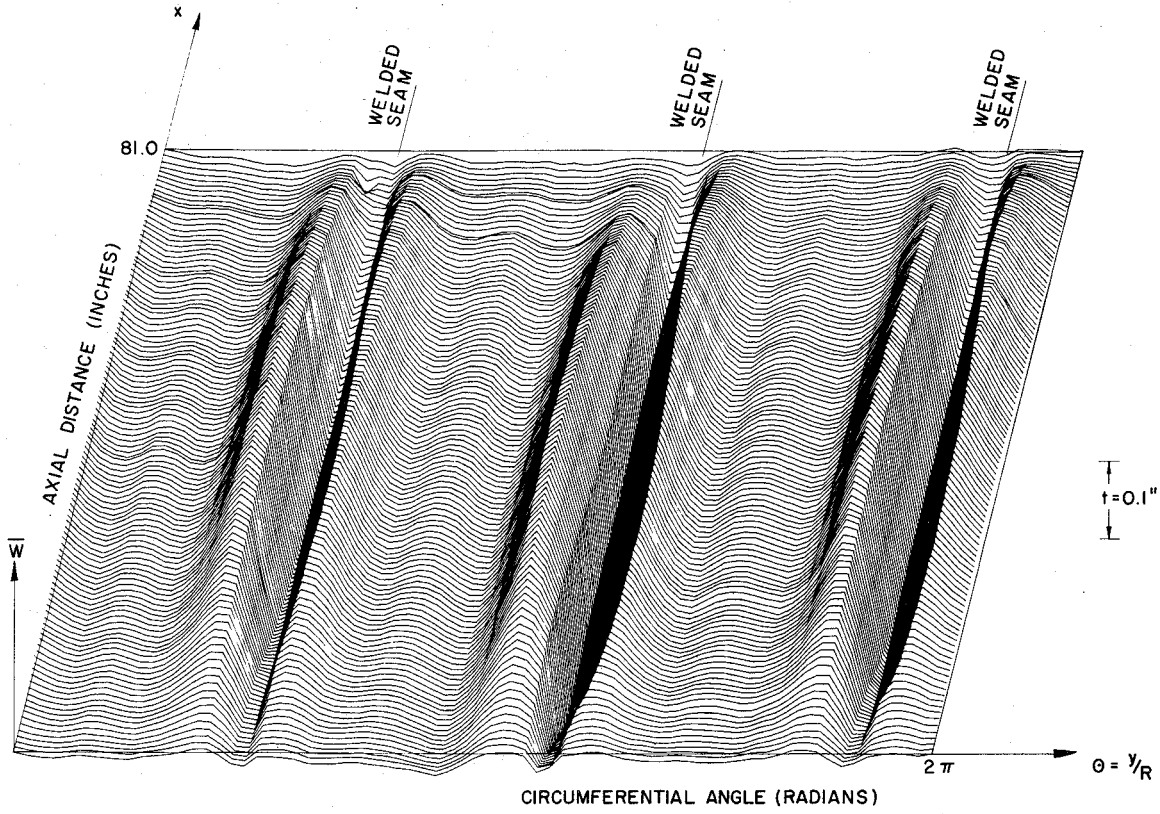

Fig. 4 Measured initial shape of the 10-ft-diam integrally stiffened shell.

with respect to the newly found "perfect" cylinder. The harmonic components of two different double Fourier series representations were also calculated.

Test Results and Discussions

Results of the imperfection surveys have been displayed several different ways. First, the measured deviations from the "perfect" shell were used to prepare a three-dimensional plot of the initial imperfections. As can be seen from Fig. 4, the longitudinal weld seams have produced a very characteristic initial imperfection consisting of a half-wave in the axial direction and nine full waves in the circumferential direction, with the imperfection amplitudes greatest at the location of the weld seams. The maximum peak-to-peak imperfection is equal to about one wall thickness (0.10 in.). As reported in Ref. 5, the same maximum peak-to-peak imperfection amplitudes were observed on laboratory scale stringer stiffened shells.

The coefficients of the following two double Fourier series

$$\bar{w}(x,y) = t\bar{W}(x,y) = t\sum_{i=0}^{N} A_{io}\cos\frac{i\pi x}{L} + t\sum\sum_{k,\ell=0}^{N}\cos\frac{k\pi x}{L}\left(A_{k\ell}\cos\frac{\ell y}{R} + B_{k\ell}\sin\frac{\ell y}{R}\right) \quad (1)$$

and

$$\bar{w}(x,y) = t\bar{W}(x,y) = t\sum\sum_{k,\ell=0}^{N}\sin\frac{k\pi x}{L}\left(C_{k\ell}\cos\frac{\ell y}{R} + D_{k\ell}\sin\frac{\ell y}{R}\right) \quad (2)$$

which were computed numerically, are displayed in Tables 2 and 3. For clearer representation any amplitude smaller than $0.005\ t$ ($=0.0005$ in.) was replaced by zero. These calculated coefficients confirm the predominance of an initial imperfection with one half-wave in the axial direction and nine full waves in the circumferential direction.

Figure 5 shows the variation of the calculated half-wave cosine Fourier coefficients as a function of the circumferential wave number ℓ for selected axial half-wave numbers k, whereas Fig. 6 shows similar plots for the half-

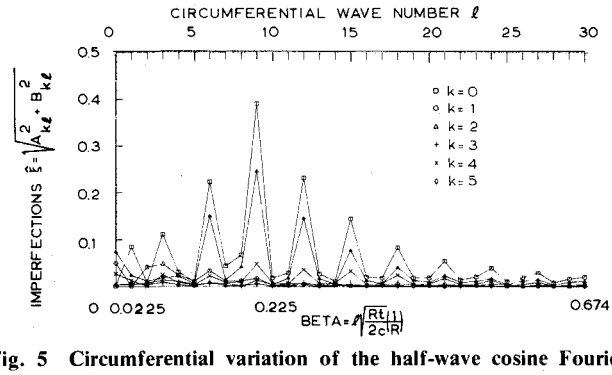

Fig. 5 Circumferential variation of the half-wave cosine Fourier representation.

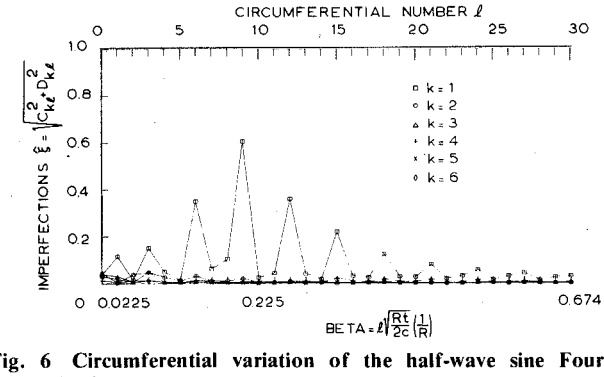

Fig. 6 Circumferential variation of the half-wave sine Fourier representation.

Table 2 Fourier coefficients of the half-wave cosine axial representation

$A_{k\ell}$ COMPONENTS $- \cos\frac{k\pi x}{L}\cos\frac{\ell y}{R}$

$\ell=$	0	1	2	3	4	5	6	7	8	9	10	11	12	13	14	15	16	17	18	19
k= 0	0.0	0.085	0.0	0.0	0.027	0.0	0.217	-0.035	0.067	-0.202	0.0	0.009	-0.180	0.017	-0.011	0.103	0.016	-0.005	0.057	-0.015
k= 1	0.050	0.0	0.0	-0.044	0.0	0.0	0.007	0.0	0.011	0.017	0.0	0.0	0.0	0.0	0.0	0.0	0.0	0.0	0.0	0.0
k= 2	-0.074	-0.017	0.0	0.006	-0.016	0.0	-0.142	0.012	-0.042	0.127	0.0	0.0	0.114	0.0	0.005	-0.053	-0.013	0.0	-0.030	0.0
k= 3	0.0	0.0	-0.005	0.009	0.0	0.0	0.0	-0.007	0.0	-0.011	0.0	0.0	-0.008	0.0	0.0	0.0	0.0	0.0	0.0	0.0
k= 4	-0.027	-0.008	0.0	0.0	-0.007	0.0	-0.022	0.008	-0.009	0.023	0.0	0.0	0.028	-0.006	0.008	-0.025	0.0	0.0	-0.015	0.0
k= 5	0.0	0.0	0.0	0.009	0.0	0.0	0.0	0.0	0.0	-0.006	0.0	0.0	0.0	0.0	0.0	0.0	0.0	0.0	0.0	0.0
k= 6	-0.017	-0.006	0.0	0.0	0.0	0.0	-0.007	0.0	0.0	0.008	0.0	0.0	0.007	0.0	0.0	0.0	0.0	0.0	0.0	0.0
k= 7	0.0	0.0	0.0	0.006	0.0	0.0	0.0	0.0	0.0	0.0	0.0	0.0	0.0	0.0	0.0	0.0	0.0	0.0	0.0	0.0
k= 8	-0.009	-0.005	0.0	0.0	0.0	0.0	0.0	0.0	0.0	0.0	0.0	0.0	0.0	0.0	0.0	0.0	0.0	0.0	0.0	0.0
k= 9	0.0	0.0	0.0	0.0	0.0	0.0	0.0	0.0	0.0	0.0	0.0	0.0	0.0	0.0	0.0	0.0	0.0	0.0	0.0	0.0
k=10	0.0	0.0	0.0	0.0	0.0	0.0	0.0	0.0	0.0	0.0	0.0	0.0	0.0	0.0	0.0	0.0	0.0	0.0	0.0	0.0

$B_{k\ell}$ COMPONENTS $- \cos\frac{k\pi x}{L}\sin\frac{\ell y}{R}$

$\ell=$	0	1	2	3	4	5	6	7	8	9	10	11	12	13	14	15	16	17	18	19
k= 0	—	0.0	0.007	-0.111	-0.016	0.008	-0.054	-0.027	0.010	-0.335	0.019	-0.027	0.147	0.021	0.0	0.101	-0.014	0.018	-0.061	-0.011
k= 1	—	0.0	0.042	-0.021	0.024	-0.011	0.033	-0.012	0.006	0.0	0.0	-0.006	0.0	0.0	0.007	0.0	0.0	0.0	-0.006	0.0
k= 2	—	-0.016	-0.011	0.018	0.015	0.0	0.049	0.009	0.0	0.211	0.0	0.018	-0.091	-0.016	0.0	-0.056	0.0	-0.005	0.028	0.013
k= 3	—	0.0	-0.006	0.010	-0.011	0.0	-0.005	0.0	0.0	-0.007	0.0	0.0	0.0	0.0	0.0	0.005	0.0	0.0	0.0	0.0
k= 4	—	-0.010	0.0	0.025	0.0	0.0	0.006	0.0	0.0	0.042	-0.007	0.006	-0.023	0.0	0.0	-0.022	0.005	-0.007	0.020	0.0
k= 5	—	0.006	0.0	0.0	0.0	0.0	-0.008	0.0	0.0	0.0	0.0	0.0	0.0	0.0	0.0	0.0	0.0	0.0	0.0	0.0
k= 6	—	0.0	0.0	0.011	0.0	0.0	0.0	0.0	0.0	0.014	0.0	0.0	0.0	0.0	0.0	0.0	0.0	0.0	0.0	0.0
k= 7	—	0.0	0.0	0.0	0.0	0.0	0.0	0.0	0.0	0.0	0.0	0.0	0.0	0.0	0.0	0.0	0.0	0.0	0.0	0.0
k= 8	—	0.0	0.0	0.008	0.0	0.0	0.0	0.0	0.0	0.007	0.0	0.0	0.0	0.0	0.0	0.0	0.0	0.0	0.0	0.0
k= 9	—	0.0	0.0	0.0	0.0	0.0	0.0	0.0	0.0	0.0	0.0	0.0	0.0	0.0	0.0	0.0	0.0	0.0	0.0	0.0
k=10	—	0.0	0.0	0.0	0.0	0.0	0.0	0.0	0.0	0.0	0.0	0.0	0.0	0.0	0.0	0.0	0.0	0.0	0.0	0.0

Table 3 Fourier coefficients of the half-wave sine axial representation

$C_{k\ell}$ COMPONENTS $- \sin\frac{k\pi x}{L}\cos\frac{\ell y}{R}$

$\ell=$	0	1	2	3	4	5	6	7	8	9	10	11	12	13	14	15	16	17	18	19
k= 1	0.036	0.116	0.0	0.0	0.041	0.0	0.339	-0.051	0.103	-0.314	0.0	0.012	-0.281	0.024	-0.018	0.156	0.027	-0.008	0.086	-0.022
k= 2	0.044	0.0	0.006	-0.043	0.0	0.0	0.0	0.0	0.010	0.021	0.0	0.0	0.007	0.0	0.0	0.0	0.0	0.0	0.0	0.0
k= 3	-0.038	0.029	0.0	0.0	0.0	0.0	0.0	-0.011	0.0	0.0	0.0	0.005	-0.006	0.008	-0.006	0.018	0.0	0.0	0.010	-0.006
k= 4	0.012	0.0	0.0	-0.014	0.0	0.0	0.006	-0.005	0.0	0.0	0.0	0.0	0.0	0.0	0.0	0.0	0.0	0.0	0.0	0.0
k= 5	-0.030	0.015	0.0	0.0	0.0	0.005	0.0	0.0	0.0	0.0	0.0	0.0	0.0	0.0	0.0	0.0	0.0	0.0	0.0	0.0
k= 6	0.015	0.0	0.0	0.0	0.0	0.0	0.0	0.0	0.0	0.0	0.0	0.0	0.0	0.0	0.0	0.0	0.0	0.0	0.0	0.0
k= 7	-0.028	0.009	0.0	0.0	0.0	0.0	0.0	0.0	0.0	0.0	0.0	0.0	0.0	0.0	0.0	0.0	0.0	0.0	0.0	0.0
k= 8	0.006	0.0	0.0	0.0	0.0	0.0	0.0	0.0	0.0	0.0	0.0	0.0	0.0	0.0	0.0	0.0	0.0	0.0	0.0	0.0
k= 9	-0.026	0.0	0.0	0.0	0.0	0.0	0.0	0.0	0.0	0.0	0.0	0.0	0.0	0.0	0.0	0.0	0.0	0.0	0.0	0.0
k=10	0.006	0.0	0.0	0.0	0.0	0.0	0.0	0.0	0.0	0.0	0.0	0.0	0.0	0.0	0.0	0.0	0.0	0.0	0.0	0.0

$D_{k\ell}$ COMPONENTS $- \sin\frac{k\pi x}{L}\sin\frac{\ell y}{R}$

$\ell=$	0	1	2	3	4	5	6	7	8	9	10	11	12	13	14	15	16	17	18	19
k= 1	—	0.008	0.014	-0.152	-0.027	0.012	-0.089	-0.039	0.014	-0.520	0.026	-0.043	0.227	0.034	0.0	0.155	-0.018	0.026	-0.092	-0.020
k= 2	—	0.0	0.039	-0.024	0.026	-0.010	0.032	-0.010	0.005	0.0	0.0	0.0	-0.006	0.0	0.008	0.0	0.0	0.0	0.0	0.0
k= 3	—	-0.007	-0.006	-0.049	0.0	0.0	0.011	-0.007	0.0	-0.007	0.009	0.0	0.006	0.0	0.0	0.013	-0.009	0.008	-0.016	0.005
k= 4	—	0.0	0.013	0.0	0.0	0.0	0.013	0.0	0.0	-0.007	0.0	0.0	0.0	0.0	0.0	0.005	0.0	0.0	0.0	0.0
k= 5	—	-0.012	0.0	-0.013	0.0	0.0	0.005	0.0	0.0	0.0	0.0	0.0	0.0	0.0	0.0	0.0	0.0	0.0	0.0	0.0
k= 6	—	0.0	0.005	0.0	0.0	0.0	0.0	0.0	0.0	0.0	0.0	0.0	0.0	0.0	0.0	0.0	0.0	0.0	0.0	0.0
k= 7	—	-0.006	0.0	-0.008	0.0	0.0	0.0	0.0	0.0	0.0	0.0	0.0	0.0	0.0	0.0	0.0	0.0	0.0	0.0	0.0
k= 8	—	0.0	0.0	0.0	0.0	0.0	0.0	0.0	0.0	0.0	0.0	0.0	0.0	0.0	0.0	0.0	0.0	0.0	0.0	0.0
k= 9	—	0.0	0.0	0.0	0.0	0.0	0.0	0.0	0.0	0.0	0.0	0.0	0.0	0.0	0.0	0.0	0.0	0.0	0.0	0.0
k=10	—	0.0	0.0	0.0	0.0	0.0	0.0	0.0	0.0	0.0	0.0	0.0	0.0	0.0	0.0	0.0	0.0	0.0	0.0	0.0

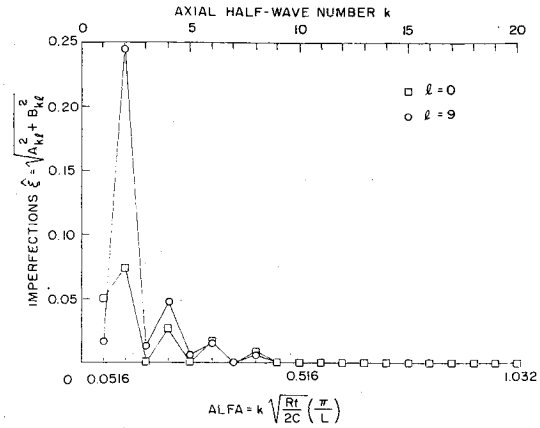

Fig. 7 Axial variation of the half-wave cosine Fourier representation.

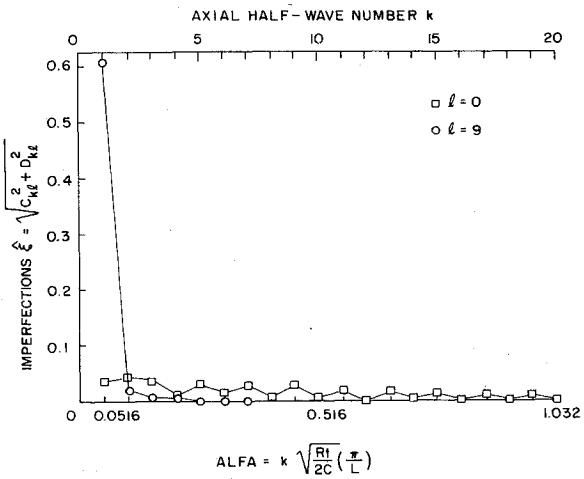

Fig. 8 Axial variation of the half-wave sine Fourier representation.

wave sine Fourier coefficients. By computing the respective mean imperfection amplitudes $\hat{\xi}$ the phase shift in the circumferential direction is eliminated. Once again the characteristic imperfection produced by the three axial weld seams used in building the shell is clearly evident, since the plots are dominated by the Fourier coefficients, which are multiples of 3. A comparison of the plots shown in Figs. 5 and 6 further indicates that the half-wave sine axial representation is superior to the half-wave cosine axial representation, since it can reproduce the main features of the measured initial imperfection survey with fewer Fourier components.

This last statement is further reinforced by the results shown in the next two figures. Figure 7 displays the variation of the calculated half-wave cosine Fourier components as a function of the axial half-wave number k for $\ell=0$ (axisymmetric components), and for $\ell=9$ (nine full waves in the circumferential direction). Figure 8, however, shows similar plots for the half-wave sine Fourier representation. As indicated by the rate of decay of the amplitudes with increasing axial half-wave numbers k, for the axisymmetric components ($\ell=0$) the half-wave cosine and for the asymmetric components ($\ell=g$) the half-wave sine axial representation is better.

For those who prefer to work with randomly distributed imperfections, Fig. 9 shows on a logarithmic scale the nondimensional discrete axisymmetric ($\ell=0$) power-spectral-density (PSD) functions plotted as a function of a nondimensional spatial frequency $\omega=k/i_{c\ell}$ (see the Appendix for the necessary derivations). Notice that only a few low-frequency components of the half-wave Fourier cosine

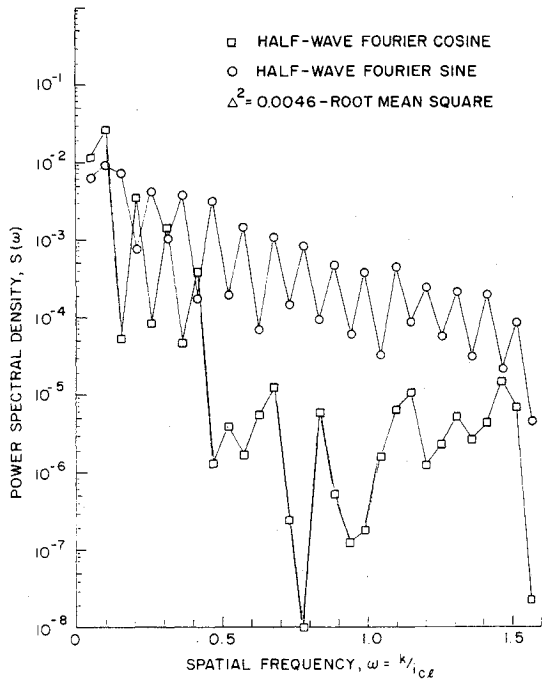

Fig. 9 Discrete axial power spectrum for $\ell=0$ (axisymmetric).

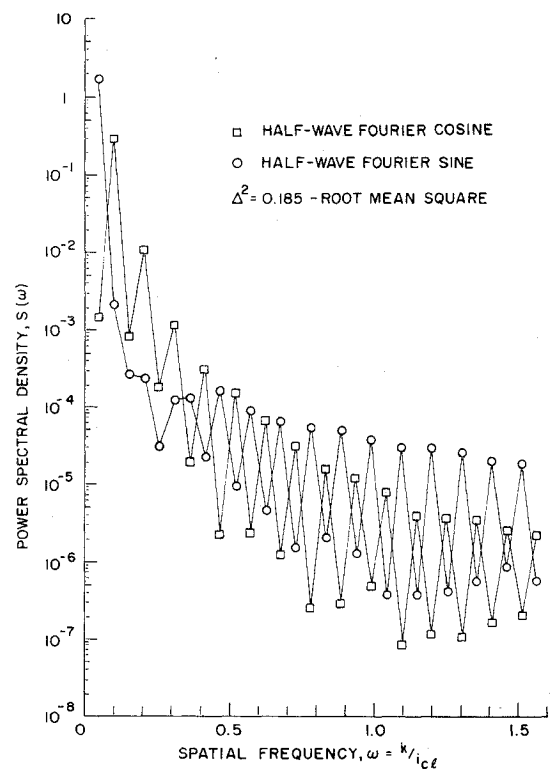

Fig. 10 Discrete axial power spectrum for $\ell=9$ (asymmetric).

representation are within one decade of each other, whereas the half-wave Fourier sine expansion also has many higher frequency components with significant amplitudes. This also confirms the statement made previously that for the axisymmetric imperfections the half-wave cosine axial representation is more suitable; that is, it represents adequately the significant features of the measured imperfections with fewer Fourier components. The nondimensional discrete axial power-spectral-density functions for the asymmetric components with nine circumferential waves are shown in Fig. 10. In this case the half-wave Fourier sine representation is the more suitable one, because by using

it all but the lowest frequency components are insignificant. The zig-zag nature of the PSD functions shown is due to the fact that in the axial direction the measured initial imperfections are essentially symmetric with respect to the middle plane of the shell. The root-mean-square value of the measured imperfections for $\ell=0$ and $\ell=9$ is given on the respective figures.

Theoretical Analysis

Based on the measured initial imperfections, one can calculate the expected buckling load by using either STAGS,[1] a two-dimensional shell type code, or by the so-called Multi-Mode Analysis.[2] Both cases have been used successfully in the past to calculate buckling loads for axially compressed imperfect cylindrical shells. In a recent paper,[6] it has been proposed to use the simpler Multi-Mode Analysis for calculating the effect of the initial imperfections and then to take into account the effect of the appropriate boundary conditions by a simple normalization procedure. This method shall be used here in order to estimate the effect of the measured imperfections.

Buckling Load Calculations by the Multi-Mode Analysis

A detailed description of this solution method is presented in Ref. 2. To introduce the initial imperfection, the analysis uses the following double Fourier series:

$$\bar{w}(\bar{x},\bar{y}) = t\sum_{i=0}^{N_1} \bar{W}_{io}\cos i\bar{x} + t\sum_{k,\ell=1}^{N_2}\sum \sin k\bar{x}\,(\bar{W}_{k\ell}\cos\ell\bar{y} + \bar{W}'_{k\ell}\sin\ell\bar{y}) \qquad (3)$$

where

$$\bar{x}=\pi x/L \qquad \bar{y}=y/R$$

The amplitudes of the harmonic components are selected from the values given in Tables 2 and 3. The circumferential phase-shifts are eliminated by working with the equivalent amplitudes defined in the Appendix. Since the number of modes included in the analysis is limited by practical considerations, the question arises: "How does one decide which of the many harmonic components are important and hence must be included in the analysis?"

Previous studies with axially compressed cylindrical shells[2,7] have shown that imperfections dominate the behavior of the shell if at or close to the lowest eigenvalue the corresponding modes have significant initial amplitudes. Conversely, imperfections do not play such a significant role if at or close to the lowest eigenvalue the corresponding modes have no significant initial amplitudes. Hence one must always consider the distribution of the eigenvalues for a given shell structure and the amplitudes of the Fourier coefficients of the measured initial imperfections simultaneously.

Table 4 shows the normalized buckling loads for the shell under consideration. These eigenvalues were computed using a membrane prebuckling analysis with the classical simply supported boundary conditions ($N_x=v=w=M_x=0$), and they are normalized by the lowest buckling load $N_{xSS-3}=2864.7$ lb/in. This buckling load corresponds to a buckling mode with one half-wave in the axial direction and eight full waves in the circumferential direction. Comparing the distribution of eigenvalues (or buckling loads) with the initial amplitudes of the corresponding eigenfunctions (or Fourier coefficients) shown in Table 3, one expects that since there are significant initial imperfections close to the (1,8) mode the calculated buckling load of the real (or imperfect) shell will be considerably lower than the corresponding classical value obtained for the perfect shell. Results of buckling load calculations using the Multi-Mode Analysis Method[12] are summarized in Table 5. In this table, the notation (2,0) denotes an axisymmetric mode with two half-waves in the axial direction, whereas (1,8) stands for an asymmetric mode with a single half-wave in the axial direction and eight full waves in the circumferential direction. In selecting additional modes, besides the magnitude of the initial imperfection and the relative size of the corresponding eigenvalue, special attention must be given to the satisfaction of the axial and circumferential coupling conditions.

It has been shown[8] that for the degenerate case of one axisymmetric $(i,0)$ and one asymmetric mode (k,ℓ) there is a single coupling relation $i=2k$. Furthermore, it has been found that coupling between three asymmetric modes with wavenumbers (k,ℓ), (m,n), and (p,q) will occur if the relations $k+m+p=$ odd integer and $q=|\ell\pm n|$ are satisfied. If these coupling conditions are satisfied, the resulting load of the shell will be lower than the buckling load with each mode considered separately.

The results of Table 5 indicate that the inclusion of properly chosen additional modes leads to decreasing buckling loads. That is, in going from a 2-mode to a 7-mode solution, the addition of five new modes resulted in a 11% decrease of the predicted buckling loads. For the 14-mode solution, the inclusion of seven additional modes produced a further 10% decrease; however, for the 21-mode solution the addition of seven new modes resulted only in a further 2% decrease of the predicted buckling load. This behavior suggests that there is a point beyond which the addition of more modes will not ne-

Table 4 Buckling loads from linear theory using classical simply supported boundary conditions ($N_x=v=w=M_x=0$)

ℓ=	0	1	2	3	4	5	6	7	8	9	10	11	12	13	14	15	16	17	18
k= 1	79.54	51.03	22.43	10.02	4.84	2.56	1.53	1.10	1.00	1.11	1.39	1.84	2.46	3.26	4.29	5.55	7.10	8.96	11.17
k= 2	20.78	18.24	13.14	8.65	5.57	3.63	2.44	1.73	1.31	1.10	1.03	1.05	1.17	1.36	1.62	1.96	2.37	2.87	3.46
k= 3	10.26	9.66	8.19	6.48	4.94	3.73	2.85	2.22	1.80	1.53	1.38	1.31	1.31	1.37	1.48	1.64	1.84	2.09	2.39
k= 4	6.99	6.77	6.18	5.39	4.57	3.82	3.21	2.72	2.36	2.10	1.93	1.83	1.79	1.80	1.85	1.94	2.07	2.23	2.43
k= 5	5.95	5.84	5.54	5.11	4.62	4.14	3.71	3.34	3.04	2.81	2.64	2.54	2.48	2.46	2.49	2.54	2.63	2.75	2.89
k= 6	5.87	5.81	5.63	5.36	5.05	4.72	4.40	4.11	3.87	3.67	3.52	3.41	3.34	3.31	3.32	3.35	3.42	3.51	3.62
k= 7	6.33	6.29	6.17	6.00	5.78	5.54	5.29	5.07	4.86	4.69	4.55	4.45	4.38	4.34	4.33	4.35	4.40	4.47	4.56
k= 8	7.16	7.13	7.05	6.92	6.76	6.57	6.38	6.20	6.02	5.87	5.75	5.65	5.57	5.53	5.51	5.52	5.55	5.61	5.69
k= 9	8.27	8.25	8.18	8.08	7.96	7.81	7.65	7.50	7.35	7.22	7.10	7.01	6.93	6.89	6.86	6.86	6.88	6.92	6.99
k=10	9.61	9.59	9.54	9.46	9.36	9.24	9.11	8.98	8.85	8.73	8.62	8.53	8.46	8.40	8.37	8.36	8.38	8.41	8.46

NORMALIZING FACTOR : $N_{xSS-3}=2864.7$ LB/IN.

Table 5 Buckling loads calculated by the multimode analysis

No. of modes	ρ_s
2-modes	
(2,0) + (1,8)	= 0.887
(2,0) + (1,9)	= 0.806
4-modes	
(2,0) + (1,8) + (1,9) + (1,17)	= 0.792
7-modes	
(2,0) + (1,7) + (1,8) + (1,9) + (1,2) + (1,15) + (1,17)	= 0.778
9-modes	
(2,0) + (1,6) + (1,7) + (1,8) + (1,9) + (1,2) + (1,13) + (1,15) + (1,17)	= 0.754
14-modes	
(2,0) + (1,6) + (1,7) + (1,8) + (1,9) + (1,12) + (1,2) + (1,3) + (1,4) + (1,5) + (1,13) + (1,15) + (1,17) + (1,18)	= 0.682
21-modes	
(2,0) + (1,6) + (1,7) + (1,8) + (1,9) + (1,10) + (1,11) + (1,12) + (1,13) + (1,14) (1,15) + (1,2) + (1,3) + (1,4) + (1,5) + (1,17) + (1,18) + (1,21) + (1,24) + (1,27) + (1,36)	= 0.655

cessarily result in a further significant decrease of the predicted buckling load. Here the estimated lower limit of $\rho_s = 0.62$ compares favorably with available large scale stiffened shell buckling test data on similar shells of $\rho_{exp} = 0.63\text{-}0.73$.[9]

Conclusions

The three-dimensional plot of the measured initial imperfections seems to indicate that the details of design of a shell and the chosen manufacturing process can decisively influence the expected distribution of the initial imperfections. In the case of the present specimen, the three axial weld seams produced an imperfection dominated by modes with one half-wave in the axial direction and multiples of three full waves in the circumferential direction. As can be seen from the plots of the Fourier coefficients, the largest component has nine full waves in the circumferential direction, practically coinciding with the lowest buckling mode of the shell.

The fact that unknowingly the shell parameters were chosen such that the lowest buckling loads and the corresponding buckling modes do coincide with the region of largest size imperfections resulted in a large calculated decrease in the load carrying capability of the shell. Would the designer have known at the time of fixing his design parameters what type of initial imperfection distribution to expect for the chosen fabrication process, a different set of shell parameters could have been selected, such that the lowest buckling modes would have come to lie outside the region of significant size imperfections. This might have produced a shell structure whose buckling load would have been less affected by initial imperfections.

Hence we must conclude that what the designer needs is information about the type and magnitude of imperfections associated with the different manufacturing processes. Especially, one must know what effect design details, such as the location of splices, will have on the expected imperfection distribution. With this information available, the designer then can tailor the design of his shell such as to minimize the expected degree of imperfection sensitivity by ensuring that the lowest buckling loads and the region of largest imperfections do not coincide, thus leading to a more efficient design.

The work presented in this paper indicates improved performance benefits can be expected if during the design phase the imperfections representative of a particular fabrication process are taken into account. Application of this approach is currently limited by the lack of available imperfection data corresponding to various fabrication methods. Thus a basic need exists for the aerospace community to conduct imperfection measurements on test and on flight hardware and to share in the establishment of an Imperfection Data Bank. Benefits from the imperfection surveys contained in such a Data Bank would be twofold: 1) desirable manufacturing processes, design practices, and configurations could be identified; 2) possibly "design criteria" could be developed that would relax current manufacturing tolerances while raising the allowable load levels.

Appendix: Derivation of the Discrete Axial Power-Spectral-Density Representation

Using the complex Fourier representation, the axial dependence of the measured initial imperfections, for a given value of the circumferential wave number ℓ, can be expressed as

$$\bar{w}(x) = t\bar{W}(x) = t\sum_{k=-\infty}^{\infty} C_k e^{ik\bar{\omega}x} \tag{A1}$$

where

$$C_k = \frac{1}{2L}\int_{-L}^{L} \bar{W}(x) e^{-ik\bar{\omega}_o x}\,dx \tag{A2}$$

$$\bar{\omega}_o = \pi/L \tag{A3}$$

The mean square value of the imperfection is given by

$$\overline{\bar{W}(x)^2} = \frac{1}{2L}\int_{-L}^{L} \bar{W}(x)^2\,dx = \sum_{k=-\infty}^{\infty} C_k{}^2 \tag{A4}$$

Also because all imperfections are referred to the "best-fit cylinder," the mean of the measured imperfections is (at least approximately) equal to zero. That is

$$\int_{-L}^{L} \bar{W}(x)\,dx = 0 \tag{A5}$$

Similarly, one can define for the axial dependence of the measured initial imperfections, for a given value of the circumferential wave number ℓ, the following Fourier integral representation

$$\bar{w}(x) = t\bar{W}(x) = t\int_{-\infty}^{\infty} C(\bar{\omega})\, e^{i\bar{\omega}x}\,d\bar{\omega} \tag{A6}$$

where

$$C(\bar{\omega}) = \frac{1}{2\pi}\int_{-\infty}^{\infty} \bar{W}(x) e^{-i\bar{\omega}x}\,dx \tag{A7}$$

Further the PSD function $p(\tilde{\omega})$ is related to the mean square value of the imperfection by the following relationship

$$\overline{\bar{W}(x)^2} = \int_{-\infty}^{\infty} p(\tilde{\omega})\,d\tilde{\omega} = 2\int_{0}^{\infty} p(\tilde{\omega})\,d\tilde{\omega} \tag{A8}$$

where $p(\tilde{\omega})$ defines a two-sided spectrum

If one now compares, following Ref. 10, the complex Fourier series (A4) with the Fourier integral (A8) expressions of the mean square value of $\bar{W}(x)$, then it is evident that in the limit as $L \to \infty$ (or as $\tilde{\omega}_o \to 0$)

$$p(\tilde{\omega}) \approx \lim_{\tilde{\omega}_o \to 0} (C_k{}^2/\tilde{\omega}_o) \tag{A9}$$

Next let us normalize this expression such that $p(\tilde{\omega})$ becomes a dimensionless quantity. Simultaneously, let us introduce the dimensionless spatial frequency ω, defined as

$$\omega = \frac{k\tilde{\omega}_o}{\sqrt{2c/Rt}} = k\frac{\pi}{L}\sqrt{\frac{Rt}{2c}} = \frac{k}{i_{c\ell}} \tag{A10}$$

where

$$i_{c\ell} = (L/\pi)\sqrt{2c/Rt} \tag{A11}$$

is equal to the number of half-waves in the classical axisymmetric buckling mode for isotropic shells. Then

$$S(\omega) = \frac{p(\tilde{\omega})}{\sqrt{Rt/2c}} = \lim_{\tilde{\omega}_o \to 0} \frac{C_k{}^2}{\tilde{\omega}_o\sqrt{Rt/2c}} = \lim_{\tilde{\omega}_o \to 0} C_{k\ell}^2 i_{c\ell} \tag{A12}$$

Finally for the half-wave cosine or half-wave sine axial representation, at a given circumferential wave number ℓ

$$S(\omega) = \tfrac{1}{4}\hat{A}_{k\ell}^2 i_{c\ell} = \tfrac{1}{4}\hat{C}_{k\ell}^2 i_{c\ell} \tag{A13}$$

because

$$4C_{k\ell}^2 = \hat{A}_{k\ell}^2 = \hat{C}_{k\ell}^2 \tag{A14}$$

The phase shift in the circumferential direction was eliminated by defining $\hat{A}_{k\ell}$ and $\hat{B}_{k\ell}$ as follows

$$\hat{A}_{k\ell} = \sqrt{A_{k\ell}^2 + B_{k\ell}^2} \qquad \hat{C}_{k\ell} = \sqrt{C_{k\ell}^2 + D_{k\ell}^2} \tag{A15}$$

Acknowledgment

Most of the work reported in this paper was carried out during the first author's two tenures as a NASA-ASEE Summer Faculty Fellow at the NASA Langley Research Center in the summers of 1974 and 1975. This aid is gratefully acknowledged.

References

[1] Almroth, B. O., Brogan, F. A., Miller, E., Zele, F., and Peterson, H. T., "Collapse Analysis for Shell of General Shape. II. User's Manual for the STAGS-A Computer Code," Air Force Flight Dynamics Lab., Wright Patterson AFB, AFFDL-TR-71-8, March 1973.

[2] Arbocz, J. and Babcock, C. D., Jr., "Prediction of Buckling Loads Based on Experimentally Measured Initial Imperfections," *Proceedings IUTAM Symposium on Buckling of Structures*, Springer-Verlag, Heidelberg, 1976, pp. 291-311.

[3] Arbocz, J. and Babcock, C. D., Jr., "Utilization of STAGS to Determine Knockdown Factors from Measured Initial Imperfections," NASA CR (to be published).

[4] Arbocz, J. and Babcock, C. D., Jr., "The Effect of General Imperfections on the Buckling of Cylindrical Shells," *Journal of Applied Mechanics*, 1969, pp. 28-38.

[5] Singer, J., Arbocz, J. and Babcock, C. D., Jr., "Buckling of Imperfect Stiffened Cylindrical Shells under Axial Compression," *AIAA Journal*, Vol. 9, Jan. 1971, pp. 68-75.

[6] Arbocz, J. and Sechler, E. E., "On the Buckling of Stiffened Imperfect Cylindrical Shells," *AIAA Journal*, Vol. 14, Nov. 1976, pp. 1611-1617.

[7] Arbocz, J., "The Effect of Initial Imperfections on Shell Stability," *Thin Shell Structures, Theory, Experiment and Design*, (Y. C. Fung and E. E. Sechler, eds.) Prentice-Hall, Englewood Cliffs, N.J., 1974.

[8] Arbocz, J. and Babcock, C. D., Jr., "A Multimode Analysis for Calculating Buckling Loads of Imperfect Cylindrical Shells," GALCIT Report SM 74-4, California Institute of Technology, Pasadena, Calif., 1974.

[9] Babel, H. W., Christensen, R. H., and Dixon, H. H., "Design, Fracture Control, Fabrication, and Testing of Pressurized Space-Vehicle Structures," *Thin Shell Structures, Theory, Experiment and Design*, (Y. C. Fung and E. E. Sechler, eds.) Prentice-Hall, Englewood Cliffs, N.J., 1974.

[10] Tennyson, R. C., Muggeridge, D. B., and Caswell, R. D., "Buckling of Circular Cylindrical Shells Having Axisymmetric Imperfection Distributions," *AIAA Journal*, Vol. 9, May 1971, pp. 924-930.